Simplified phase-recovery method in temporal speckle pattern interferometry

Pablo Etchepareborda,[1,*] Arturo Bianchetti,[1] Ana Laura Vadnjal,[1] Alejandro Federico,[1] and Guillermo H. Kaufmann[2]

[1]Electrónica e Informática, Instituto Nacional de Tecnología Industrial, P.O. Box B1650WAB, B1650KNA San Martín, Argentina

[2]Instituto de Física Rosario and Centro Internacional Franco Argentino de Ciencias de la Información y de Sistemas, Blvd. 27 de Febrero 210 bis, S2000EZP Rosario, Argentina

*Corresponding author: pabloe@inti.gov.ar

Received 6 August 2014; accepted 11 September 2014;
posted 17 September 2014 (Doc. ID 220496); published 17 October 2014

A simplified method for object phase recovering is implemented in temporal speckle pattern interferometry when the employed interferometer admits the introduction of a temporal carrier, and the well-known two-beam interferometry equation is verified. The spatiotemporal evolution of the object phase is isolated by modulating the acquired interferometric intensity signals with a known temporal carrier in order to carry out its analysis by using a bivariate empirical mode decomposition framework that avoids the application of the Hilbert transform, which is not suitable for intensity signals with abrupt fluctuations. The advantages and limitations of this technique are analyzed and discussed by comparing computation time and phase recovery capability with well-known phase-retrieval methods by means of numerical simulations and experimental data.

OCIS codes: (100.2000) Digital image processing; (100.5070) Phase retrieval; (100.3010) Image reconstruction techniques; (120.5050) Phase measurement; (120.6150) Speckle imaging.
http://dx.doi.org/10.1364/AO.53.007120

1. Introduction

Speckle interferometry (SI) allows noncontact, whole field, and high sensitivity measurements of mechanical displacement fields in optically rough objects subjected to dynamic deformations. In SI measurement systems, different digital processing techniques are used to retrieve the spatiotemporal information of the optical phase concealed in speckle pattern interferogram images, which is related to the mechanical displacement fields. In practice, the most commonly used methods for phase retrieval are based on 2D fringe analysis [1]. Spatial carriers are introduced in the interferometer, and the implementation of bidimensional Fourier analysis allows one to recover the optical phase associated with displacement fields. Phase-shifting techniques also were introduced [2,3], in which three or more different images are acquired for each state of deformation by imposing phase steps in the reference beam between the camera captures. It is well known that these conventional techniques involve inherent limitations when low errors and high dynamic measurement performance are required. Temporal speckle pattern interferometry (TSPI) methods are suitable candidates because these can be better adapted to dynamic SI measurement systems. In the TSPI approach, a known temporal carrier is introduced, and the phase recovery analysis is performed temporarily for each pixel. Several 1D signals containing the temporal history of the intensity pixel are analyzed separately. Therefore, unwrapping errors due to the presence of unwanted noisy and low modulated pixels are

1559-128X/14/307120-09$15.00/0

diminished significantly compared with methods that rely on 2D and 3D unwrapping procedures. In addition, the TSPI approach can remove the limitation of the inherent correlation length that traditional techniques suffer when speckle interferometric signals are spatially analyzed. TSPI methods achieve accuracy, robustness, and are fast when the optical setup is available with fast actuators and imaging sensors [4].

In this work, the spatial intensity distribution measured at the CCD sensor is described by the two-beam interferometry equation $I(t) = I_0(t) + I_M(t)\cos[\Delta\phi(t)]$, where $I_0(t)$ is the background intensity, $I_M(t)$ is the modulation intensity, and $\Delta\phi(t) = \phi_o(t) - \phi_r(t)$ is the phase difference between the phase of the temporal carrier $\phi_r(t)$ and the object phase to be recovered $\phi_o(t)$. Note that the position of the analyzed pixel in the horizontal and vertical directions was intentionally omitted for clarity. In this two-beam interferometry approach, TSPI methods exploit different properties of the signal $I(t)$ intending to isolate the modulated intensity term while removing the presence of the background intensity for object phase recovery. The most popular TSPI method is based on the Fourier transform (FT) and uses a bandpass filter to obtain a complex signal with its phase equal to $\Delta\phi(t)$ [5]. The bandwidth (BW) and central frequency of this filter should be tuned at every instant of the sequence to improve noise robustness. This nontrivial task encouraged the use of the windowed FT and the wavelet transform (WT) to automatize the filter selection by keeping only the ridge of the transformed signals for further analysis, which retrieves the object phase [6,7]. Fu *et al.* presented two variants: the phase gradient method that performs integration over the values of the local frequencies where the ridge takes place, and the method of the phase of the transformed signal, which uses the arctangent function to obtain the wrapped object phase. Even though the phase gradient method avoids the use of a phase unwrapping process, the phase errors accumulated during the integration procedure favor high deviations in the obtained results [8].

A different point of view to recover phase information was recently introduced by using the analytic method (AM), which takes the phase of the analytic function obtained by means of a Hilbert transform of the zero-mean modulated term in the two-beam interferometry equation [9]. The AM requires removing the background intensity with an averaging filter that needs proper estimation of its kernel, especially when the signal spectrum covers a large spectral bandwidth. Actually, temporal speckle interferometric signals possess intrinsic difficulties such as abrupt fluctuations, and the linear filtering methods become a defective framework of analysis. Recently, the empirical mode decomposition (EMD) was included in the AM (EMD+AM) to cope with background suppression in the multicomponent real valued $I(t)$ with an automatic and adaptive data-driven filtering [10–12], which requires the usual application of the Hilbert transform. However, by multiplying $I(t)$ by the complex term $\exp[i\phi_r(t)]$, $(i^2 = -1)$, before any filtering process, the original EMD algorithm can be extended to a bivariate frame in order to satisfy the necessity of analyzing a complex-valued time series [13]. The use of the Hilbert transform is then naturally avoided by using this new decomposition. Thus, a simplified phase-recovery method that improves the phase recovery performance for a wide set of working conditions is achieved.

In the following section, we briefly review the EMD algorithm and explain its purpose in EMD+AM for better understanding of the differences with the bivariate analysis used in the proposed method. Afterward, we show numerical and experimental results, analyze the performance of the proposed method, and derive conclusions.

2. Theoretical Analysis

EMD makes use of the intuitive concept of oscillation. A continuous sequence of oscillations with an equal number of extrema and zero-crossing points forms a mode of oscillation that can be linked to a particular time scale. The EMD algorithm empirically decomposes the data as a set of superimposed modes of oscillations and one trend signal. This decomposition adaptively derives its own set of basis functions by extracting different modes of oscillation directly from the data. An extracted oscillation mode is named the intrinsic mode function (IMF) when it has a zero mean envelope at any point, which is defined by the mean of the upper and lower envelopes resulting from the interpolation of local maxima and minima, respectively [14]. An iterative process named *sifting* is used to obtain the composing IMF of a given signal $s(t)$. Each sifting process extracts the fastest oscillating IMF from the residual signal, which is obtained by subtracting the already extracted IMF from the original signal. This algorithm involves a configurable maximum number of iterations or a stopping criterion threshold that determines if the IMF being sifted out achieves the condition of zero mean envelope. This threshold parameter should be set considering that signals conformed by many scales of oscillations need more sifting precision and, therefore, a lower threshold level. The EMD algorithm can be stopped at step J with the extraction of the IMF $c_J(t)$ and residue $r_J(t)$, especially if the last residue found is a monotonic trend signal. Thus, the EMD method obtains the following signal decomposition:

$$s(t) = \sum_{j=1}^{J} c_n(t) + r_J(t). \tag{1}$$

The issue of border effects should be taken into account to minimize propagation errors due to finite observation lengths. Rilling *et al.* showed that good results are obtained by simply mirroring the extrema

close to the edges before envelope interpolations [15]. The selection of IMF to remove from the decomposition in Eq. (1) is determinant to improve the temporal and frequency resolution of the local frequency analysis carried out by the AM [14]. This is done depending on the carrier frequency and the bandwidth of the modulated intensity [11]. In the method of EMD+AM evaluated in this work, only the first IMF of the decomposition of $I(t)$ is held to implement the AM on a fast oscillating signal [12].

In the proposed phase recovery method, we rearrange the interferometric equation by multiplying both sides of the equality by the complex phase term associated with the temporal carrier to obtain

$$(I - I_0)e^{i\phi_r} = \frac{I_M}{2}[e^{i\phi_o} + e^{-i(\phi_o - 2\phi_r)}], \tag{2}$$

where the spatiotemporal dependence was omitted for clarity. Two distinctive terms arise at the right of Eq. (2). The first term only contains the object phase ϕ_o, which is the quantity of interest. In the second one, $\psi \equiv 2\phi_r - \phi_o$, the object phase is subtracted by the double of the carrier phase. Therefore, it is easy to distinguish two different characteristic time scales between those terms, since the variations imposed by the object phase are much slower than the phase changes given by ψ. It is important to note that the temporal evolution of ϕ_o is highly determinant of the performance of the phase recovery process since fast temporal variations of ϕ_o should produce a superposition between characteristic time-frequency scales.

In the complex plane, the temporal evolution of the real and imaginary parts of the bivariate time series $z(t) \equiv [I(t) - I_0(t)]\exp[i\phi_r(t)]$ are assimilated to the Cartesian coordinates of a point moving in a 2D space. The two highlighted terms shown in Eq. (2) are represented in the 2D space as the superposition of the fast rotation given by $\psi(t)$ over a slower one corresponding to $\phi_o(t)$. The bivariate analysis decomposes $z(t)$ into rotational terms. The bivariate EMD algorithm (BivEMD) proposed in Ref. 13 adapts the rationale underlying the analysis of oscillations in EMD to the bivariate case of *rotations* (do not confuse with bidimensional EMD). Therefore, the two superimposed rotational terms can be effectively identified and separated by the application of the BivEMD to the left-hand side of Eq. (2) by estimating $I_0(t)$ in advance.

The main structure of the algorithm of the BivEMD is similar to the EMD since the same decomposition model presented in Eq. (1) is considered for the complex signal $z(t)$. In this new context, the complex rotating components $c_j(t)$ are named bivariate intrinsic mode functions (BIMF), which are sifted out from $z(t)$ in descending order of rotational speed until the expected amount of BIMFs is reached or no more rotating components can be driven from the last residue obtained by subtracting the already sifted BIMFs from $z(t)$. In order to extract the BIMF $c_j(t)$, the bivariate sifting process iteratively subtracts the slowest rotations from the residue $r_{j-1}(t)$ until they are no longer detectable. Note the similarity with EMD sifting that iterates by subtracting the slowly oscillating mean envelopes to refine the IMF. As maximum and minimum envelopes cannot be defined for complex signals, a 3D tube that encloses the signal is used in BivEMD sifting. The center of the enclosing tube delineates a slowly rotating signal in the 3D space that shall be subtracted at each iteration from the BIMF being extracted. In order to find this tube, the complex signal is projected on K different directions to obtain 1D real signals. The extrema of these signals are then detected to find upper and lower envelopes using a piecewise cubic Hermite interpolating polynomial (PCHIP) [16]. In [13], two ways of defining the mean signal of the 3D tube are given, and we used the second scheme with $K = 4$ directions defined by the angles $\phi_k \in \{0, \pi/2, \pi, 3\pi/4\}$ rad. This scheme considers the ellipse formed by the slice of the tube corresponding to each instant of the sequence. The intersection of two straight lines, one being halfway between the two horizontal tangents of the ellipse, and the other line being halfway between the vertical tangents, shows the path of the mean signal. When K is even, the algorithm of the sifting operation $c_j(t) = \mathcal{S}[r_{j-1}(t)]$ can be briefly formulated by means of the following steps:

1. Set $c_j(t) = r_{j-1}(t)$.
2. **repeat**
3. **for** $1 \le k \le K/2$ **do**
4. Project complex $c_j(t)$ on direction ϕ_k to obtain real $p_k(t) = \Re\{e^{-i\phi_k}c_j(t)\}$
5. Identify all extrema in $p_k(t)$ and mirror border extrema
6. Interpolate all maxima to obtain envelope $e_{\max}(t)$ and minima to obtain $e_{\min}(t)$
7. Compute mean envelope $m_k(t) = [e_{\max}(t) + e_{\min}(t)]/2$
8. Subtract from projection to end up with partial estimate on direction ϕ_k, $s_k(t) = p_k(t) - m_k(t)$
9. **end for**
10. Compute new estimate $c_j(t) = \frac{4}{K}\sum_{k=1}^{K/2} e^{i\phi_k}s_k(t)$
11. **until all** $|m_k(t)|$ are below a stopping criterion threshold

In step 4, $\Re$ is the real part of $\{\cdot\}$. Note that steps 5 to 8 are the same steps as the well-known sifting operation in 1D EMD but carried out over the projections $p_k(t)$. In this scheme, we only use data information from the projections to define the envelopes and find the slowly rotating signal. If more information from $c_j(t)$ were used in step 8, the algorithm would be more prone to sampling errors since the uncertainty of the envelope points grows, especially near the projected extrema [13]. By construction, the BivEMD algorithm adaptively decomposes $z(t)$ into a finite set of J BIMFs with different time-scale rotations and one trending residue. This empirical and adaptive separation mechanism allows us to properly select and sum the BIMF that isolate the rotational term of $\phi_o(t)$ in Eq. (2). Subsequently, the object phase is recovered by means

of the *arctan* function. A simple 1D temporal phase unwrapping can be performed for each pixel of the CCD sensor to obtain the temporal evolution of the phase. Fast C versions of MATLAB functions for EMD and BivEMD algorithms are available via a web link in [13].

The complete algorithm of the proposed TSPI method can be summarized as follows:

1. **for all** intensity evolutions of the (m,n) pixels, $I(m,n,t)$ **do**
2. Estimate background intensity $I_0^{\text{est}}(m,n,t)$
3. Subtract $I_0^{\text{est}}(m,n,t)$ from $I(m,n,t)$
4. Multiply by the complex carrier to get $z(t) = e^{\phi_r}[I(m,n,t) - I_0^{\text{est}}(m,n,t)]$
5. Decompose $z(t)$ using BivEMD
6. Remove the first BIMF, $\tilde{z}(t) = \sum_{n=2}^{N} c_n(t)$
7. Take the phase of $\tilde{z}(t)$ and unwrap to get the estimated object phase $\hat{\phi}_o^{\text{est}}(m,n,t)$
8. Subtract initial random speckle phase, e.g., $\phi_o^{\text{est}}(m,n,t) = \hat{\phi}_o^{\text{est}}(m,n,t) - \hat{\phi}_o^{\text{est}}(m,n,t_{\text{initial}})$
9. **end for**

Step 2 can be found by a variety of methods such as fitting a constant or linear trend or a smoothing cubic spline to $I(m,n,t)$. In step 4, we use the known phase of the carrier ϕ_r to perform the complex modulation. Steps 5 and 6 can be reduced to one single step if only the first BIMF is extracted so that the residue becomes $\tilde{z}(t)$. In step 8, the random speckle phase is subtracted to make the phase measurements relative to the state of deformation at time t_{initial}. Unwrapping methods sometimes solve this constant error by making the phase relative to the mean phase estimated along a first frames window in which the sample was kept unchanged [17], especially if the recovered phase presents border effects at the first frames.

It is important to note that Eq. (2) also can be modified to

$$Ie^{i\phi_r} = I_0 e^{i\phi_r} + \frac{I_M}{2}[e^{i\phi_o} + e^{-i(\phi_o - 2\phi_r)}]. \tag{3}$$

In that case, if the Fourier spectra of $I_M \exp(i\phi_o)$ and $I_0 \exp(i\phi_r)$ are not superposed, then the BivEMD method can be used to obtain ϕ_o even if I_0 is not subtracted from I before multiplying by $\exp(i\phi_r)$. Thus, we obtain an even more simplified approach that implies a reduced computational effort since the estimation of I_0 is avoided. However, as the BivEMD algorithm has to be applied to a signal that implicitly contains more components, the threshold parameter for the sifting stopping criterion needs to be lowered in order to obtain a correct decomposition. This results in more sifting iterations and computational time, especially with low modulated pixels. At first, we suggest to use 10 sifting iterations. If the BivEMD algorithm does not obtain the expected amount of BIMFs, a very low stopping criterion threshold should be used. These simplifications of the method are intended to reduce errors and accelerate its implementation.

3. Numerical Results

To evaluate the performance of the BivEMD phase recovery method, several sequences of N_T frames, each containing $N \times N$ intensity pixels of speckle interferograms were generated using a simulation method commonly adopted in the assessment of phase recovery algorithms [5]. In this simulation, the carrier modulation is imposed over the reference arm of the interferometer, and the expression for the generation of interferograms is given by

$$I(m,n,t) = A(t)^2|Re^{i\alpha + i\theta(t)} + \mathcal{F}^{-1}\{H(u,v) \times \mathcal{F}\{e^{i\phi_o(m,n,t)}U(m,n,t)\}\}|^2, \tag{4}$$

where $A(t)$ is the spatial mean amplitude of the simulated object beam, proportional to the laser beam amplitude. R is a relation of amplitude between the reference and the object beams and α is the phase difference between the two beams. $\mathcal{F}\{\cdot\}$ and $\mathcal{F}^{-1}\{\cdot\}$ are the operators of 2D fast FT and inverse fast FT, respectively. The phase of the reference beam is determined by the introduction of the temporal carrier $\theta(t)$, which is a periodic sequence that follows phase steps of $[0; \pi/2; \pi; -\pi/2]$ radians sequentially. The spatiotemporal evolution of the object phase is represented by $\phi_o(m,n,t)$, with integers $1 \le m, n \le N$ and $1 \le t \le N_T$. $U(m,n,1)$ is a matrix of random complex numbers with phase uniformly distributed in the interval $[-\pi, \pi)$ radians and unitary amplitude. $H(u,v)$ denotes a circular low-pass filter in the Fourier plane with radius $a \le N/2$, which sets the average speckle size $s_o = N/(2a)$. In this work, we adopted $s_o = 1.1$ to ensure proper simulation of small grains of speckle.

The reference beam was simulated with an amplitude four times larger than the spatial mean amplitude of the signal corresponding to the object beam. The simulation of speckle interferogram sequences was obtained by performing the operations in Eq. (4) using double precision variables. Several possible sources of noise were simulated to analyze the robustness of the different tested phase-retrieval methods. Our noise model was based on the following equations:

$$\theta(t) = t\frac{\pi}{2}[1 + \eta_C(t)], \tag{5}$$

$$A(t) = A_0[1 + f(t)], \tag{6}$$

$$U(m,n,t+1) = U(m,n,t)\exp[i\eta_L(m,n,t)], \tag{7}$$

$$I_{\text{CCD}}(m,n,t) = I(m,n,t) + \eta_{\text{CCD}}(m,n,t). \tag{8}$$

The inaccuracy of the actuator that generated the carrier was simulated according to Eq. (5), where η_C is a Gaussian random variable with standard deviation σ_C. The quality of the interferograms affected by instability of amplitude was described by Eq. (6), where $f(t) = K_L \sin(t\pi/N_T)$ was arbitrarily

chosen as one lobe of a sine function, and the parameter K_L controlled the magnitude of the amplitude instability. By introducing Eq. (7), phase masks are permanently added to achieve speckle pattern decorrelation being $\eta_L(m,n,t)$ a Gaussian random phase variation with standard deviation σ_L. Equation (8) modeled CCD read noise with the addition of Gaussian noise images $\eta_{\mathrm{CCD}}(m,n,t)$ with standard deviation σ_{CCD}. Subsequently, the resulting intensities were converted to 8-bit values to simulate the digitizing process in a low-resolution CCD sensor.

A spatiotemporal object phase evolution was assigned to all the pixels in a sequence of images, according to Eq. (9):

$$\phi_o(m,n,t) = K_E \phi_{sp}(m,n)\delta(t), \tag{9}$$

where K_E is a simulation parameter, the spatial distribution of deformation $\phi_{sp}(m,n)$ is designed as shown in Fig. 1(a), and $\delta(t)$ is a 1D temporal phase step with damped oscillation [see Fig. 1(b)]. Note in Fig. 1 that the extreme values of $\phi_{sp}(m,n)$ and $\delta(t)$ make K_E to set the maximum excursion of phase evolution $\hat{E}_\phi = \max_{m,n}[E_\phi(m,n)]$ with pixel excursions $E_\phi(m,n) = \max_t[\phi_o(m,n,t)] - \min_t[\phi_o(m,n,t)]$. We used the notation $\max_k[(k)]$ as the maximum (k) for all valid arguments k. This choice of $\phi_o(m,n,t)$ obtains dissimilar temporal phase variations within the same field of analysis.

The solid black curve in Fig. 2 shows the temporal evolution of the original object phase at an arbitrarily selected pixel, which is compared with the results of the evolution of the unwrapped recovered phase for the methods of fast BivEMD and PCHIP interpolation, wavelet transform (WT), EMD+AM and FT method with narrowband (BW $= \pi/16$) and broadband (BW $= \pi/8$) filters. In order to assess the performance of fast implementations of the methods, they were applied directly to the temporal intensity signals, without any previous border treatment of $I(t)$. The resulting 1D temporal signals were unwrapped so that a possible unwanted phase offset could be set to zero by subtracting the mean resulting phase at 10 initial frames with no border effects. Thus, we obtained readable curves of evolution of the phase at a single pixel for every method. In Fig. 2(a), we show the evolution of the retrieved phase for a case of low levels of noise and good quality of the laser ($\sigma_C = 0$, $K_L = 0$, $\sigma_L = 0$, $\sigma_{\mathrm{CCD}} = 0.9$), giving a sequence of SNR $= 32$ dB. Almost every method proved to recover the correct phase in the whole phase evolution. The FT method with a narrowband filter showed severe phase-recovery disengagements. In Fig. 2(b), a simulated case of SNR $= 10$ dB, noise levels achievable with common cameras and exposure times were used to test the methods in the case of having a more demanding environment or low-quality acquisition equipment ($\sigma_C = 0.05$, $K_L = 0.4$, $\sigma_L = 0.05$, $\sigma_{\mathrm{CCD}} = 7$). The resulting phase evolutions showed higher error. Only the BivEMD method with PCHIP interpolation retrieved the correct phase

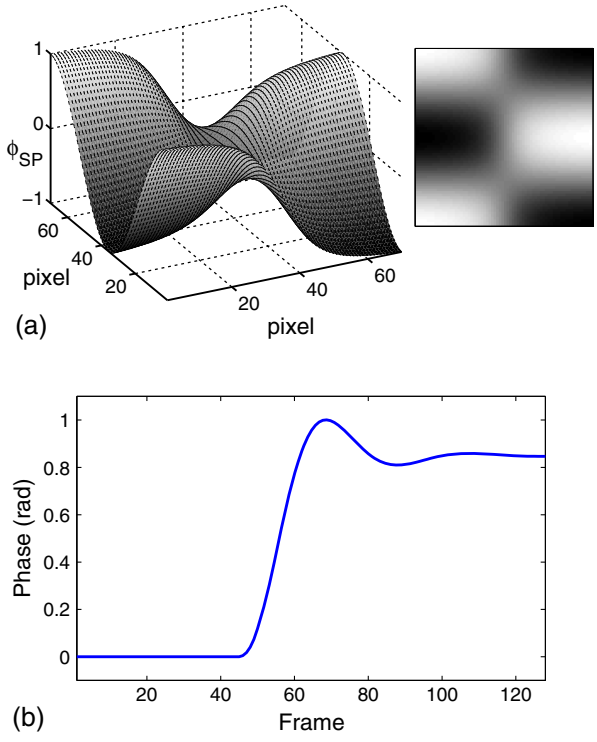

Fig. 1. (a) 3D representation and phase image of spatial distribution of deformation $\phi_{sp}(m,n)$. (b) Simulated 1 rad excursion phase step, $\delta(t)$.

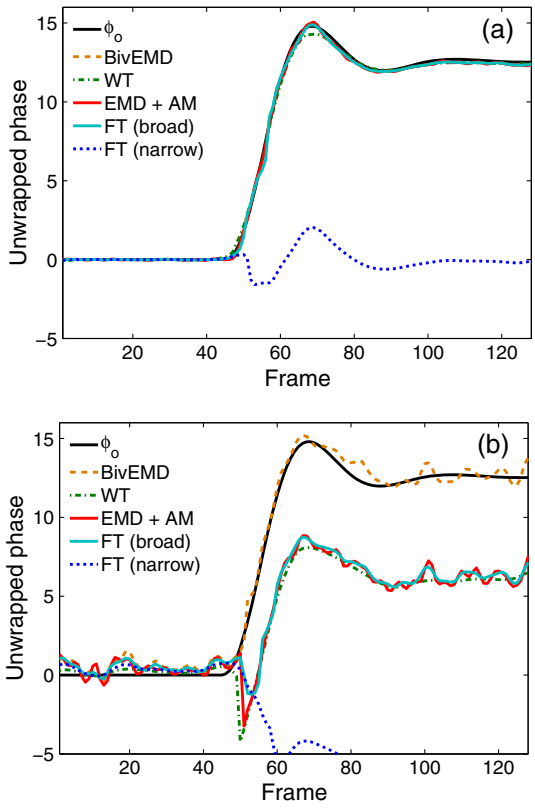

Fig. 2. Original and retrieved temporal evolution of phase at a given pixel for a simulated sequence of interferograms: (a) SNR $= 32$ dB and (b) SNR $= 10$ dB.

evolution, showing no disengagements for this particular pixel. In the following, we present a more thorough characterization of the performance of these methods.

The spatial distortion of phase images between the original object phase and the recovered phase was analyzed by using the structural similarity (SSIM) index [18]. The distortion measured by the SSIM is associated to loss of correlation, undesired offset of mean phase, or alteration of standard deviation. A quality factor $Q(t)$ is obtained at each frame t in the range of values $[-1, 1]$, where $Q(t) = 1$ is satisfied for exact phase retrieval. By using a sliding window approach, for every spatial translation j, $Q_j(t)$ is calculated locally by means of the relation:

$$Q_j = \frac{2(2\bar{\phi}_o\bar{\phi_o^{\text{est}}} + C_Q)(\sigma_{\phi_o\phi_o^{\text{est}}} + C_Q)}{(\bar{\phi}_o^2 + \bar{\phi_o^{\text{est}}}^2 + C_Q)(\sigma_{\phi_o}^2 + \sigma_{\phi_o^{\text{est}}}^2 + 2C_Q)}, \quad (10)$$

where σ_{ϕ_o} and $\sigma_{\phi_o^{\text{est}}}$ are standard deviations of ϕ_o and ϕ_o^{est}, respectively; $\sigma_{\phi_o\phi_o^{\text{est}}}$ is the correlation coefficient between ϕ_o and ϕ_o^{est}; $\bar{\phi}_o$ and $\bar{\phi_o^{\text{est}}}$ are the means of both portions of the images, and C_Q is a small positive constant that avoids numerical instability for near zero sample means, variances, or correlations. Note that the number of frame dependence was omitted for clarity. The SSIM index $Q(t)$ is obtained by calculating the average of all local $Q_j(t)$. The constant $C_Q = 0.01$ was fixed to achieve similar values of Q along the temporal sequence for all simulations.

In Fig. 3(a), we show the spatial distribution of the unwrapped original object phase at frame 100 $\phi_o(m, n, 100)$, adopting $\tilde{E}_\phi = 20$ rad. The values of phase were represented from white to black in gray scale for the interval $[-16, 16]$ radians. Figure 3(b) presents the phase retrieved by the BivEMD method for the SNR = 32 dB case at frame 100 using PCHIP for envelope interpolation. In Figs. 3(c) and 3(d), we show the resulting phase images at the same frame by using WT and FT with broadband filter methods. In practice, a median filter is usually applied for removing noisy pixels, and that effect is shown in Fig. 3(e) with the filtered result of the BivEMD method from Fig. 3(b). The SSIM index obtained for the image in Fig. 3(b) was $Q(100) = 0.749$, and the filtered result in Fig. 3(e) obtained $Q^{\text{filt}}(100) = 0.961$. In Figs. 3(f)–3(h), the median filtering results for BivEMD, WT, and FT method with broadband filter are shown, in that order, for direct visual comparison of the results for the SNR = 10 dB case. The obtained SSIM indices are $Q(100) = 0.646$ for BivEMD, $Q(100) = 0.630$ for WT, and $Q(100) = 0.539$ for the FT method. The BivEMD method obtained clean images, presenting a low amount of noise due to phase disengagements and high accuracy of phase recovery, especially in pixels with $E_\phi(m, n) > 2\pi$. In the low SNR case, the filtered results showed gray zones in areas where pixels with phase disengagements appeared more frequently. BivEMD obtained a filtered phase image with smaller gray zones.

In Fig. 4, we plot the temporal evolutions of the SSIM index computed for the two analyzed noisy cases. These results correspond to the average SSIM indices obtained from an ensemble of 20 simulations for each SNR case. BivEMD proved to be the best method to retrieve phase after the occurrence of the object phase step given by $\delta(t)$. The robustness of BivEMD method to different sources of noise is exhibited by noticing the results shown in Figs. 4(a) and 4(b). As expected, the SSIM indices from the high

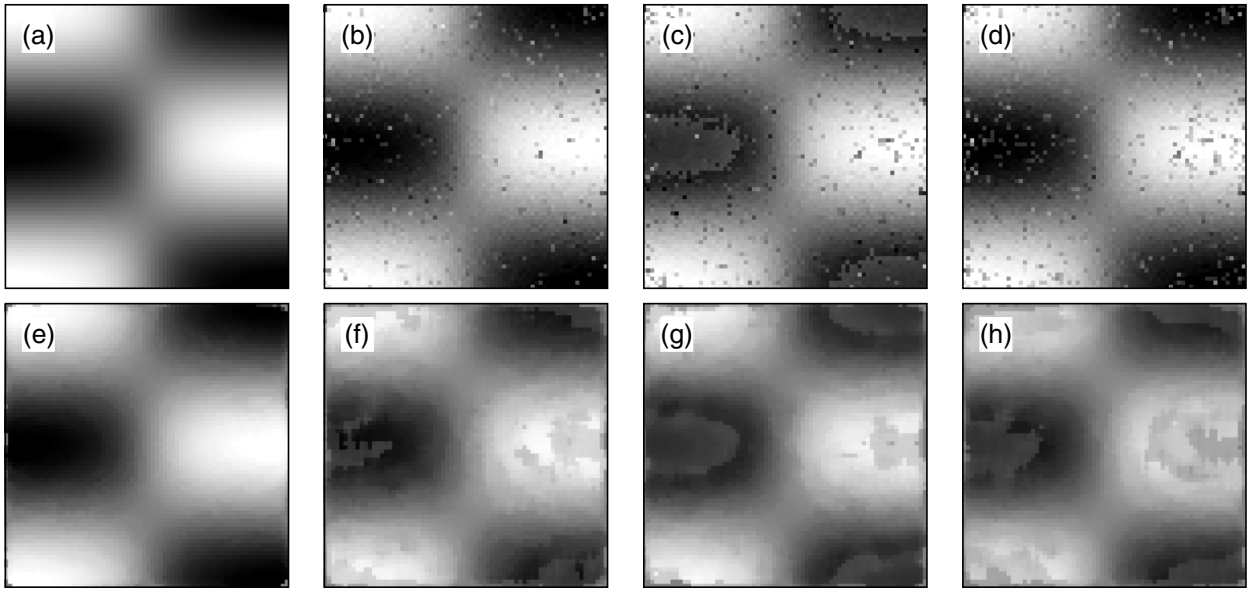

Fig. 3. (a) Simulated $\phi_o(m, n, 100)$, 70 × 70 pixels spatial distribution of object phase at frame 100 (original phase). Spatial distribution of retrieved phase at frame 100 for cases (b)–(e) SNR = 32 dB and (f)–(h) SNR = 10 dB: (b) BivEMD method with PCHIP interpolation; (c) WT method; (d) FT with broadband filter; (e) median filtering for (b); (f) median filtering BivEMD (PCHIP) method; (g) median filtering WT method; (h) median filtering FT (broadband) method.

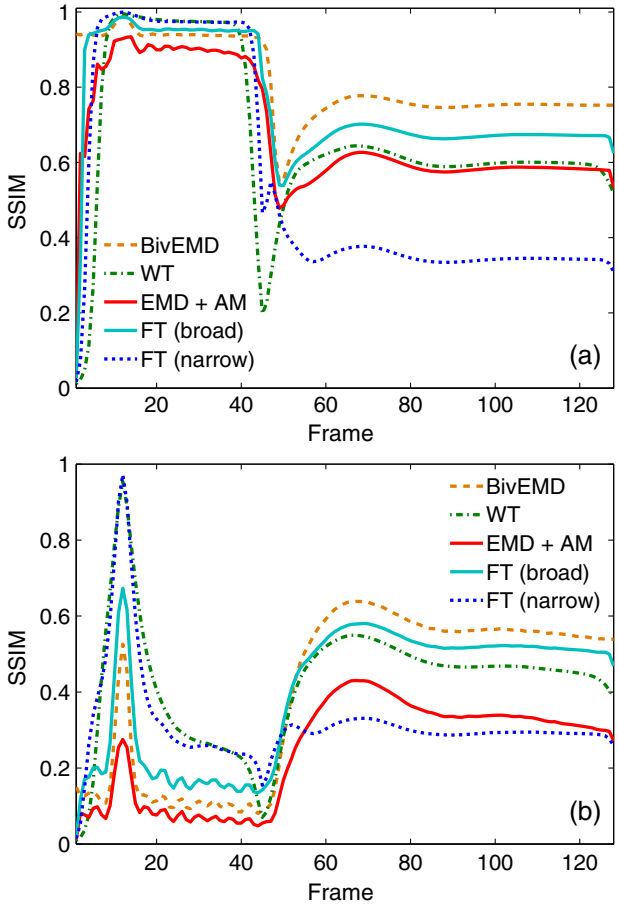

Fig. 4. Temporal evolution of SSIM index for the retrieved phases for the simulations with (a) SNR = 32 dB and (b) SNR = 10 dB.

Table 1. Mean Elapsed Time of TSPI Phase-Retrieval Methods with $N = 70$ and $N_T = 128$

Method	Elapsed Time (s)
BivEMD (PCHIP)	1.8
BivEMD (ZOH)	1.5
WT	4.2
EMD+AM	2.3
FT (narrow)	1.5
FT (broad)	1.5

SNR simulation were higher than the SSIM indices corresponding to the low SNR case. EMD+AM obtained the worst noise robustness, showing a decay of the SSIM index in relation to other methods when the SNR of the simulation was lowered from 32 to 10 dB. We also note that the simple border treatment in the BivEMD method for mirroring borders at the sifting procedure was enough to obtain high SSIM indices at the border frames of the sequence. The high peak of the SSIM index at the first frames in Fig. 4(b) is due to the subtraction of the initial random speckle phase by means of a first frames window analysis [17].

The average elapsed times of each method are presented in Table 1. We used C implementations of the methods interfaced with MATLAB scripts and ran in a 2.93 GHz CPU. The results show that FT analysis is the fastest phase-retrieval method, and the WT method is considerably slower than the other methods. Although PCHIP interpolation was used in a BivEMD algorithm, we remark that the interpolation method can be simplified up to a zero-order hold (ZOH) interpolation that considerably reduces computation time at a low cost of SSIM index for low noise situations.

In Table 2, we show the temporal mean of SSIM indices for a special region of interest (ROI) for frames 45–90. This region removes the retrieved phase at the temporal borders of the simulations and the first frames that have no phase variations. An intermediate SNR = 15 dB case is added to this table using $\sigma_C = 0.01$, $K_L = 0.2$, $\sigma_L = 0.025$, and $\sigma_{\mathrm{CCD}} = 3.5$. Also, a case with a lower excursion of object phase was assessed using maximum excursion $\hat{E}_\phi = 7$ rad for the simulation. We observe that the SSIM indices for BivEMD are always better than the rest of the employed methods for the high excursion case. BivEMD showed high versatility to recover phase evolutions that correctly follow different rates of object phase variations within the same sequence of images. In the case of $\hat{E}_\phi = 7$ rad, there was no demand on versatility, and the best tuned method obtained the best performance for each SNR situation; thus, BivEMD, WT, and FT with narrowband filter methods being the most appropriate methods for these cases.

4. Experimental Results

To illustrate the performance of the BivEMD phase-recovery method, we continue by analyzing the TSPI data obtained from the out-of-plane deflection of a

Table 2. Temporal Mean Values of SSIM Within ROI

SNR	32 dB		15 dB		10 dB	
	$\hat{E}_\phi$ in radians					
Method	7	20	7	20	7	20
BivEMD (PCHIP)	0.68	0.74	0.55	0.65	0.36	0.52
BivEMD (ZOH)	0.66	0.70	0.44	0.56	0.19	0.36
WT	0.64	0.57	0.56	0.54	0.42	0.45
EMD+AM	0.66	0.59	0.48	0.49	0.24	0.33
FT (broad)	0.68	0.67	0.58	0.60	0.43	0.49
FT (narrow)	0.65	0.38	0.58	0.34	0.49	0.30

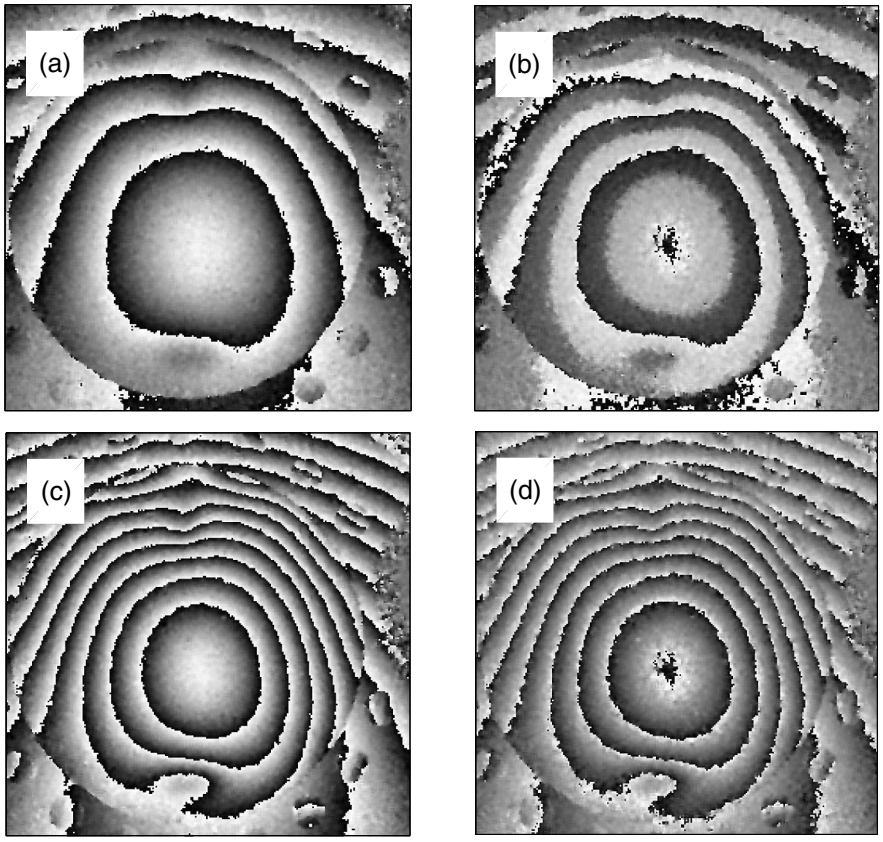

Fig. 5. Wrapped object phase distributions corresponding to the frame numbers 200 in (a) and (b); 500 in (c) and (d). Left column corresponds to the phase recovered by using the BivEMD method and right column by FT method.

flawed specimen submitted to a thermal wave. In this experiment, 512 frames composed by interferometric speckle pattern images of 256×256 pixel were acquired. The object under test was an aluminum circular plate of 10 cm diameter and 2 mm thick, clamped along its edge. Two flaws in the form of flat-bottomed slots were milled into the upper and lower back surface of the plate. Within a conventional out-of-plane TSPI system, a phase-modulated reference beam was combined with an object beam scattered by the specimen. The resulting beam was registered with a high-frame-rate digital camera. The reference beam was passed through a Pockels cell, which was driven by a staircase waveform generator following a repetitive cycle of 4 temporal equally spaced voltage levels to produce the phase-shift values of $\{0, \pi/2, \pi, 3\pi/2\}$, which act as a temporal carrier. Interested readers can read the details of this experiment in Ref. 5. This optical setup allows direct comparison between the TSPI phase recovery procedures by observing the retrieved object phase distribution.

A prefiltering process is usually applied to reduce the effects of low modulated pixels when interferometric speckle pattern signals are analyzed [12]. However, in this work we have not preprocessed the data for better understanding of the differences in performance between the phase-recovery methods. The methods compared in the previous section

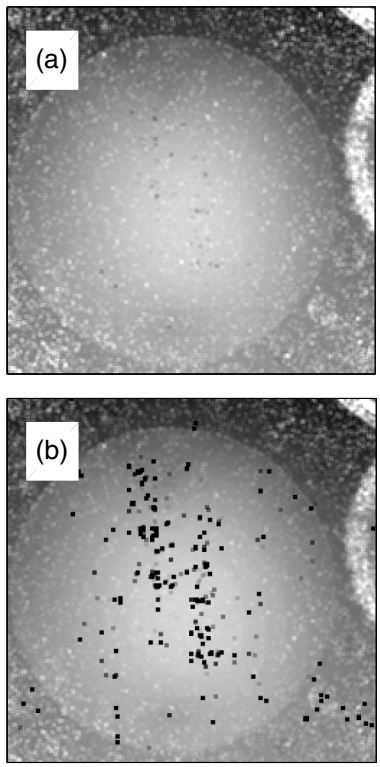

Fig. 6. Unwrapped object phase distributions corresponding to the frame number 500 obtained by method: (a) BivEMD; (b) FT. The gray-scale maps the phase interval $[-50, 50]$ rad.

were applied over the speckle sequence. In Fig. 5, we show the recovered object phase of BivEMD and FT methods corresponding to the frame numbers 200 and 500. The bandwidth of the filter used in the FT method was tuned to obtain the best achievable phase images for an experimented observer. We note that quite good reproducibility is obtained with both methods, and, consequently, the flaws located in the specimen are completely characterized. The phase is wrapped in the $[-\pi, \pi)$ radians interval and linearly mapped to gray-scale images. The fast BivEMD method showed much cleaner results than the phase obtained by FT method.

A simple 1D unwrapping process was applied to the evolution of the retrieved object phase at each pixel to obtain the total deformation at every frame. The results corresponding to frame number 500, and methods BivEMD and FT, are shown in Fig. 6. The gray scale was mapped linearly on the interval $[-50, 50]$ radians. In Fig. 6, the shape of the deformation can be straightforwardly seen. In Fig. 6(b), the pixels with phase-recovery disengagements are markedly shown by the FT method as black dots. On the contrary, in Fig. 6(a), the disengagements presented by the BivEMD are naturally concealed between other recovered phases.

5. Conclusions

In this work, we evaluated and compared the bivariate EMD as a core tool for the implementation of a simplified adapted procedure for recovering the temporal evolution of the object phase in TSPI. A considerable variety of spatiotemporal phase excursions at the object beam of the interferometry setup can be determined within this framework. The use of this complex decomposition allows us to extract the object phase evolution from a sequence of interferograms without introducing the Hilbert transform into the analysis, as it is the common procedure in the use of EMD for phase-retrieval methods. The computation time is reduced by using a single sifting process to filter out only the first BIMF of the decomposition.

The performance of BivEMD was compared with other well-known methods by using numerical simulations and by means of experimental measurements. In the numerical simulation analysis, the SSIM index was used as a holistic fidelity measure, which is appropriate for a thorough assessment of phase images retrieved by the studied methods. We found that BivEMD with PCHIP envelope interpolation is the best choice for phase recovering in TSPI, especially in cases with several rates of object phase temporal variations and levels of noise. In experimental results, use of the BivEMD procedure was the method with the best robustness to common image acquisition and processing problems and obtained trustworthy wrapped phase images.

References

1. M. Takeda, H. Ina, and S. Kobayashi, "Fourier-transform method of fringe-pattern analysis for computer-based topography and interferometry," J. Opt. Soc. Am. **72**, 156–160 (1982).
2. J. M. Kilpatrick, A. J. Moore, J. S. Barton, J. D. C. Jones, M. Reeves, and C. Buckberry, "Measurement of complex surface deformation by high-speed dynamic phase-stepped digital speckle pattern interferometry," Opt. Lett. **25**, 1068–1070 (2000).
3. D. N. Borza and I. T. Nistea, "High temporal and spatial resolution in time resolved speckle interferometry," Opt. Lasers Eng. **50**, 1075–1083 (2012).
4. I. T. Nistea and D. N. Borza, "High speed speckle interferometry for experimental analysis of dynamic phenomena," Opt. Lasers Eng. **51**, 453–459 (2013).
5. G. H. Kaufmann, "Phase measurement in temporal speckle pattern interferometry using the Fourier transform method with and without a temporal carrier," Opt. Commun. **217**, 141–149 (2003).
6. Y. Fu, R. M. Groves, G. Pedrini, and W. Osten, "Kinematic and deformation parameter measurement by spatiotemporal analysis of an interferogram sequence," Appl. Opt. **46**, 8645–8655 (2007).
7. Y. Fu, C. J. Tay, C. Quan, and H. Miao, "Wavelet analysis of speckle patterns with a temporal carrier," Appl. Opt. **44**, 959–965 (2005).
8. A. Dursun, S. Özder, and F. N. Ecevit, "Continuous wavelet transform analysis of projected fringe patterns," Meas. Sci. Technol. **15**, 1768–1772 (2004).
9. V. Madjarova, H. Kadono, and S. Toyooka, "Dynamic electronic speckle pattern interferometry (despi) phase analyses with temporal hilbert transform," Opt. Express **11**, 617–623 (2003).
10. F. A. M. Rodriguez, A. Federico, and G. H. Kaufmann, "Phase measurement improvement in temporal speckle pattern interferometry using empirical mode decomposition," Opt. Commun. **275**, 38–41 (2007).
11. F. A. M. Rodriguez, A. Federico, and G. H. Kaufmann, "Hilbert transform analysis of a time series of speckle interferograms with a temporal carrier," Appl. Opt. **47**, 1310–1316 (2008).
12. S. Equis and P. Jacquot, "The empirical mode decomposition: a must-have tool in speckle interferometry?" Opt. Express **17**, 611–623 (2009).
13. G. Rilling, P. Flandrin, P. Gonçalves, and J. Lilly, "Bivariate empirical mode decomposition," IEEE Signal Process. Lett. **14**, 936–939 (2007).
14. N. E. Huang, Z. Shen, and S. R. Long, "A new view of nonlinear water waves: the hilbert spectrum," Annu. Rev. Fluid Mech. **31**, 417–457 (1999).
15. G. Rilling, P. Flandrin, and P. Gonçalves, "On empirical mode decomposition and its algorithms," in *IEEE-EURASIP Workshop on Nonlinear Signal and Image Processing NSIP-03* (IEEE, 2003), pp. 8–11.
16. L. Shulin, Z. Haifeng, W. Hui, and M. Rui, "Application of improved EMD algorithm for the fault diagnosis of reciprocating pump valves with spring failure," in *IEEE Signal Processing and Its Applications Symposium* (IEEE, 2007), pp. 1–4.
17. P. Ruiz, J. Huntley, Y. Shen, C. Coggrave, and G. Kaufmann, "Vibration-induced phase errors in high-speed phase-shifting speckle-pattern interferometry," Appl. Opt. **40**, 2117–2125 (2001).
18. Z. Wang, A. Bovik, H. Sheikh, and E. Simoncelli, "Image quality assessment: from error visibility to structural similarity," IEEE Trans. Image Process. **13**, 600–612 (2004).